Research Square

Preprints are preliminary reports that have not undergone peer review.
They should not be considered conclusive, used to inform clinical practice,
or referenced by the media as validated information.

Sensitivity analysis of reverse engineering approaches for 3D-scanned welds with complex geometries

Xiru Wang

xiru.wang@iwm.fraunhofer.de

IWM: Fraunhofer-Institut fur Werkstoffmechanik IWM https://orcid.org/0000-0002-2586-6308

Jan Schubnell

FhG-IWM: Fraunhofer-Institut fur Werkstoffmechanik IWM

Gustav Hultgren

KTH Royal Institute of Technology: Kungliga Tekniska Hogskolan

Zuheir Barsoum

KTH Royal Institute of Technology: Kungliga Tekniska Hogskolan

Research Article

Keywords: 3D scanning, Reverse engineering approach, Weld surface geometry, Stress concentration factor, Finite element analysis

Posted Date: November 6th, 2026

DOI: https://doi.org/10.21203/rs.3.rs-11379654/v1

License: This work is licensed under a Creative Commons Attribution 4.0 International License.
Read Full License

XIII-3248-2026

Sensitivity analysis of reverse engineering approaches for 3D-scanned welds with complex geometries

Xiru Wang[1,a], Jan Schubnell [1], Gustav Hultgren [2], Zuheir Barsoum [2]

[1] Fraunhofer Institute of Mechanics of Materials IWM, Fatigue and Fracture Mechanics, Germany

[2] KTH Royal Institute of Technology, Department of Engineering Mechanics, Division of Material & Structural Mechanics, Sweden

[a] Corresponding author: xiru.wang@iwm.fraunhofer.de

Abstract

High stress concentrations are primarily caused by variations in the weld surface geometry and can lead to fatigue failure. 3D scanning technology combined with reverse engineering is becoming more widely used to capture detailed surface geometries and to build numerical models for further fatigue analysis. However, studies on the influence of different scanning systems, pointing spacing, and modeling approaches are limited. For this reason, a sensitivity analysis is needed to evaluate the reliability of the reverse engineering approach. Two scanning systems, fringe light projection (FLP) and laser line sensor (LLS), with different resolutions were applied to welded specimens with complex geometries. The stress concentration factors (SCFs) were determined using finite element analysis (FEA) based on the surface scans (point clouds). Two different modeling methods, connecting parts with tie connections or through sub modeling were compared. In addition, different element size and type, shape functions were used in the FEA. To cover the effect of near surface variation of weld quality and stress concentrations, critical distance theory (CDT) approach was applied. The results show that SCFs are more sensitive to the reverse engineering approach than CDT are.

Keywords

3D scanning, Reverse engineering approach, Weld surface geometry, Stress concentration factor, Finite element analysis

1. Introduction

Welded joints are often the fatigue-critical locations in metallic components and structures because the weld bead and particularly the weld toe act as geometric notches. The resulting notch effect leads to local stress concentrations which reduce the fatigue strength of welded joints compared to the base material and thus reduce the fatigue life of welded structures [1,2]. Numerous experimental and numerical studies have shown that the local weld geometry at the weld toe is directly related to fatigue crack initiation and fatigue life [3–7]. This relationship is commonly quantified by the stress concentration factor (SCF), defined as the ratio of the maximum local stress at the weld toe to the nominal stress in the component [8]. Reliable SCF values are therefore essential both for fatigue design and for the identification of weak points in welded components and structures.

SCFs can be obtained by finite element (FE) analyses using 2D or 3D representations of the joint geometry [9]. Although directly determining the stress concentration factor (SCF) based on the full 3D weld geometry is conceptually straightforward, such analysis entails a massive modeling and computational work, making it often difficult to implement in routine engineering practice. Consequently, most established methods rely on simplified geometric descriptions of the weld toe. Parametric solutions express the SCF as a function of a set of weld geometrical parameters, such as weld toe radius ρ, weld toe angle α, weld leglength L and plate thickness T, which are derived from idealized 2D cross-sections [10-12]. Numerous parametric equations for different joint types and load cases are available and are widely used in design recommendations and standards; however, the determination of the required geometric parameters is often difficult. The local weld toe radius and weld toe angle vary along the weld seam and depend on the evaluation method, the measurement system and the selected analysis region. Round-robin studies on the extraction of weld geometry parameters from measurements demonstrate considerable scatter between different laboratories, algorithms and operators, even for identical machined components [13,14]. As a result, SCFs computed from parametric equations reflect not only the variation of the weld geometry but also high uncertainties in parameter identification. In addition, the reduction of the true 3D weld shape to a single 2D profile and a handful of scalar parameters neglects out-of-plane variations, 3D effects, local irregularities and undercuts which may significantly influence the local stress field [15]. Comparisons between SCFs obtained from parametric equations and SCFs determined by FE simulations on measured real weld geometries have shown large difference [16,17].

Modern 3D scanning techniques now allow weld surfaces to be digitized with high spatial resolution and in short measurement times. Structured-light and laser-triangulation scanners provide point clouds of the actual weld toe geometry and are increasingly used to characterize weld quality and to extract geometric parameters [18-21]. Nevertheless, most existing approaches still use these scans only as an intermediate step to derive traditional parameters such as ρ and α, which are then inserted into parametric SCF equations or simplified FE models. In this workflow, the fundamental limitations of parameter-based methods remain, such as the necessity to idealize the weld geometry and the strong dependence of the SCF on how geometric parameters are defined and measured.

An obvious alternative is to use the scanned weld surface directly as a basis for numerical stress analysis. Several studies have used reverse engineering approach and demonstrated that FE models constructed from measured weld geometries can be used to determine SCFs more realistically [22]; however, these investigations are typically limited to a small number of welds and are based on case-specific modelling workflows. There is currently no standardized, scan-based procedure for building 3D FE models of welded joints and extracting SCFs in a general way. In particular, the influence of practical modeling and measurement choices (e.g. scanning system, point spacing, reverse engineering strategies, and modeling parameters) on the resulting SCF has not been systematically quantified. This lack of standardization makes it difficult to compare results across different studies and hinders the widespread application of scan-based SCF assessment in engineering practice.

The aim of the present work is to develop and investigate a 3D FE-based workflow for the direct determination of SCFs at welded joints using reverse engineering approach based on real geometry. The surfaces are scanned with high-resolution 3D scanners, the weld surface is reconstructed and converted into solid FE models by reverse engineering, without introducing parametric simplifications of the weld toe. The local principal stress field is evaluated along the weld toe, and the SCF is obtained as the ratio of the maximum principal stress to the nominal stress.

The paper is structured as follows. Section 2 introduces the welded specimens and the critical distance approach. Section 3 describes reverse engineering workflow and the finite element modelling, including meshing strategies, element types and loading conditions. Section 4 reports and discusses the results with respect to the influence of scan and modelling parameters on the SCF distributions. Sections 5 and 6 summarize the main findings, discuss implications for engineering practice and give recommendations for future work.

2. Methodology and specimen

2.1 Manufacturing

The fillet weld specimens investigated in this work were manufactured using a Gas Metal Arc Welding (GMAW) process. The weld configuration consisted of a double-sided transverse stiffener with a weld angle of 45°. The base material was 10 mm

thick S355 structural steel. G4Si1 filler wire with a diameter of 1.2 mm was used in accordance with DIN EN 757:1997-95. As shielding gas, M21-ArC-15 containing 15–20% CO_2 was applied at a flow rate of 15 l/min. More welding process parameters are listed in **Table 1**. To intentionally introduce local weld imperfections, the welding direction was varied, resulting in different start-stop characteristics, as illustrated in **Figure 1**. Depending on the welding sequence of the intermittent welds, end-end, start-start, and start-end positions were generated. After welding, the specimens were stress-relieved under vacuum at 560 °C for 30 minutes. X-ray diffraction measurements revealed only minor residual stresses below 10 MPa at the specimen surface. Therefore, the specimens were assumed to be residual-stress-free. The welded plates contained a continuous fillet weld with a total length of 1000 mm. After welding, the plate was cut transverse to the weld into eight individual specimens, each with a width of 120 mm. In this study, specimen No. 2 with an end-to-end configuration was selected for the sensitivity analysis. Further details are provided in **Figure 2**.

Table 1 : Welding process parameters

Voltage [V]	Currency [A]	Wire diameter [mm]	Welding Speed [mm/s]	Wire feed speed [m/min]
310	28.7	1.2	7.5	13.0

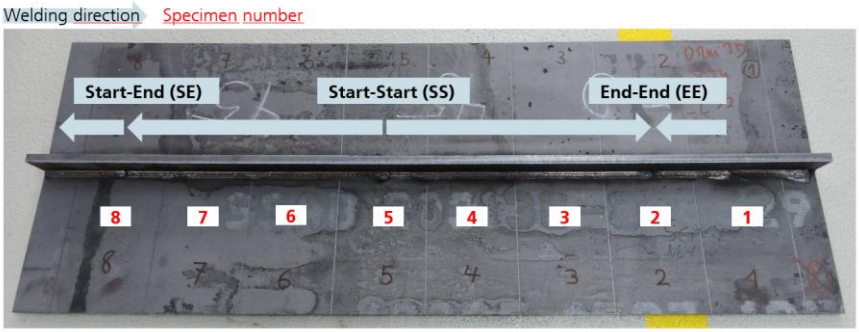


Figure 1: Specimen characteristics

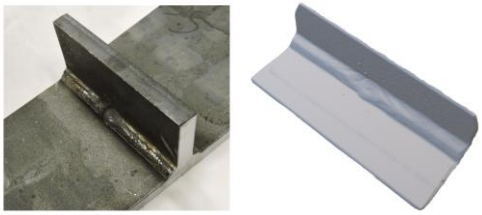


Figure 2: Weld details of specimen no.2

2.2 Critical distance approach

As demonstrated in the work of [15], the correlation between fatigue life and local weld quality appears to be weak for the investigated specimens. This suggests that local surface stress concentrations are not the dominant factor governing fatigue life. Therefore, the critical distance theory (CDT) is employed in this work to account for these surface effects. CDT, originally proposed by Peterson [23], states that stress at a material-dependent critical distance L from the most highly loaded point can be used directly to estimate fatigue strength. Later, Tanaka [24] and Taylor [25] showed that the same concept, formulated within the framework of linear-elastic fracture mechanics, can be applied to predict the fatigue strength of notched metallic components.

$$\boldsymbol{L = \frac{1}{\pi}\left(\frac{\Delta K_{th}}{\Delta \sigma_0}\right)^2} \tag{1}$$

where ΔK_{th} is the threshold range of the cyclic stress intensity factor, and $\Delta\sigma_0$ is the amplitude of the endurance limit of the material.

A simpler empirical approximation for L (in mm), as a function of the tensile strength R_m (in MPa), was proposed by Lawrence et al. [26] and Lawrence, Ho and Mazumdar [27]:

$$\boldsymbol{L = 0.0025 \left(\frac{2068}{R_m}\right)^{1.8}} \quad (2)$$

More recently, Baumgartner et al. [28] derived a linear relation between HV and L, based on best fits to fatigue tests on notched specimens representing base material and heat-affected zones of S235, S355, QStE380, S690, and S960QL:

$$\boldsymbol{L = -0.00026\, HV + 0.216} \quad (3)$$

Using these three expressions, the critical distance L was estimated as follows. The endurance limit $\Delta\sigma_0$ was determined from the FKM guideline based on a HAZ hardness of 210 HV, corresponding to a tensile strength of R_m =675 MPa according to ISO 18265. With a threshold $\Delta K_{th}(R = -1)$of 12.53 MPa (m)$^{-1/2}$ taken from the NASGRO database, equation (1) yields L =0.129 mm. Equation (2) gives L =0.187mm, and Equation (3) yields L =0.154 mm. In the simplest implementation of CDT (the point method), the stress is evaluated at a depth of $L/2$ below the surface, i.e. $\sigma(L/2)$. All three values lie within the range of typical initial crack sizes (0.05–0.10 mm) commonly assumed in linear-elastic fracture mechanics analyses.

3. Reverse engineering approach

As shown in Figure 3, the typical reverse-engineering workflow is illustrated. First, the specimen is digitized using 2D and 3D scanning techniques. In the subsequent data preparation step, the acquired data are cleaned, filtered, and processed using appropriate evaluation algorithms to reconstruct a structured surface model. Based on this geometry, a finite element (FE) model is generated to evaluate the local stress distribution and the corresponding stress concentration factors (SCFs) on the surface. The individual steps are discussed in more detail in the following subsections.

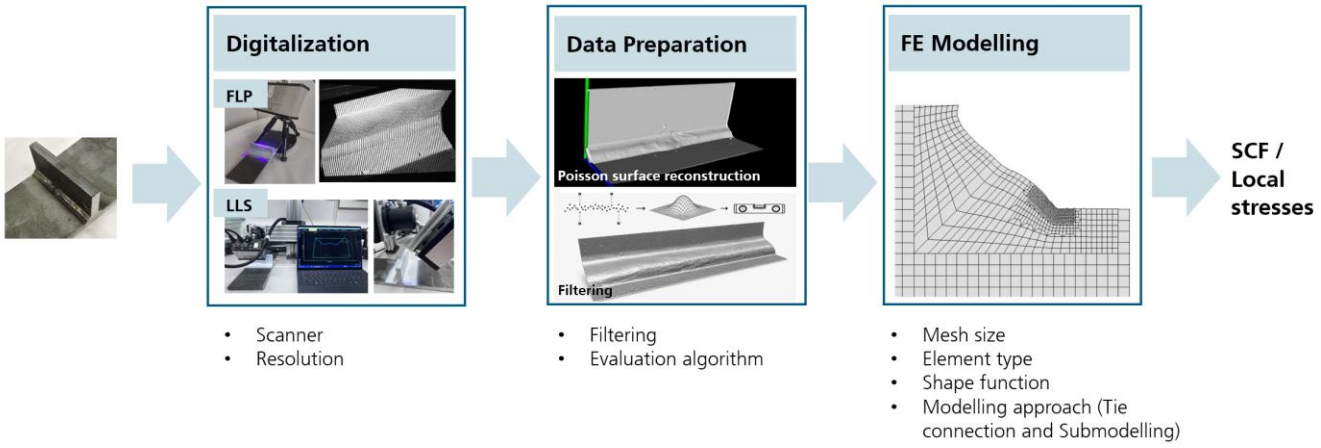


Figure 3: Reverse-engineering workflow

3.1 Digitalization

To investigate the effect of the scanning system on the reverse-engineering workflow, the surface of the fillet weld was digitized using two different scanning systems: a 3D fringe light projection (FLP) sensor (SC3500-120) and a 2D laser line sensor (LLS) (SC3050-25/BL), see Figure 3. The FLP sensor is a full-field structured-light system that captures a dense areal point cloud with almost isotropic lateral point spacing in a single shot. In this case, the specimen was coated with a thin white layer to improve surface reflectivity and scanning quality. In this study, two point spacings – 30 µm and 60 µm are conducted on the welds and are compared. In contrast, the LLS projects a focused laser line and records one profile (2D cross-section) at a time, generating a 3D dataset by moving the sensor along the weld toe. The system records 1280 measurement points per profile while the sensor is traversed along the weld at 5 mm/s; with a sampling frequency of 100

Hz this corresponds to a point spacing of approximately 50 µm in the travelling direction, following Hultgren et al. [29]. While the FLP provides a larger field of view and homogeneous meshes that are well suited for global weld geometry, the LLS offers higher local detail and depth accuracy along the weld toe, which is beneficial for resolving small radii and steep curvature. These theoretical differences in measurement principle and point spacing directly may influence the resulting mesh characteristics and must be considered when selecting mesh parameters and evaluating the reconstructed weld geometry.

3.2 Data preparation

For FLP data, the open-source software MeshLab® was used for the alignment of scans acquired with different orientations. Due to the random orientation of the scanned models, an alignment procedure was performed using the Random Sample Consensus (RANSAC) algorithm [30]. Subsequently, the discrete 3D surface representation, consisting of individual point cloud data, was converted into a continuous surface model by means of Poisson Surface Reconstruction, as proposed by Kazhdan [31]. In this study, the open-source Python implementation PoissonRecon was employed [32]; the reconstruction depth (octree depth) was selected such that the resulting effective grid size was clearly smaller than the target cross-section spacing of 0.2 mm, while the influence radius and weighting parameters were tuned to suppress high-frequency noise but preserve the weld toe geometry. Finally, cross-sectional profiles were generated from the reconstructed continuous surface by intersecting the model with a series of equidistant cutting planes and interpolating points at predefined locations with a spacing of 0.2 mm.

In contrast to the FLP data, the as-welded fillet welds were scanned using a Winteria® weld quality measurement system. [29]. Only minor filtering using the proprietary Winteria® software [29] was applied to remove obvious noise and outliers, and no global alignment or surface reconstruction was performed; cross-sectional profiles were extracted directly from the filtered line data at a spacing of 0.2 mm, consistent with the FLP-based profiles.

It is worth mentioning that, to improve the robustness of the FE model and avoid artefacts caused by edge noise at the specimen ends, 10 mm were removed from each side of the scanned specimen for the simulations, resulting in an effective simulated specimen length of 100 mm.

3.3 Finite element modelling

Based on the measured weld geometries, three-dimensional FE models of the fillet-welded specimens were generated to analyze the local stress state at the weld toe. The geometry of the weld was reconstructed from cross-sectional profiles extracted every 0.2 mm along the weld, as described in Section 3.2. Using the MATLAB code developed by Hultgren et al [33], a hexahedral-element mesh of the weld toe region was generated with two different mesh resolution, corresponding to element sizes of 0.06 and 0.12 µm, see Figure 4. These mesh sizes are consistent with the IIW recommendations for numerical simulation of weld toe details [1]. The boundary conditions were defined by constraining displacement in the global X-direction ($U_1 = 0$) while allowing transverse deformation. Axial tensile loading was applied to the opposite end surface as a uniform pressure of 1 MPa, acting along the longitudinal axis of the specimen. This configuration generated a nominal uniaxial tensile stress state, see Figure 5.

To investigate the influence of the element formulation on the predicted stress field, four different 3D solid elements were employed: the quadratic, fully integrated element, corresponding element type C3D20 in the commercial solver ABAQUS©, the quadratic, reduced-integration element (C3D20R), the linear, fully integrated element (C3D8), and the linear, reduced-integration element (C3D8R).

In addition, two different modelling strategies were applied in the 3D FE analyses to limit the total number of elements in the model: TIE connection and Sub-modeling, see Figure 5. The tie constraint was used to connect the refined weld toe mesh to the surrounding, coarser mesh by enforcing displacement compatibility across the interface without requiring matching node locations [34]. Sub-modeling was employed as a two-step approach, in which a global model with a relatively coarse mesh was analyzed first, and the resulting displacements along a cut boundary were then imposed as boundary conditions on a local submodel with a highly refined mesh around the weld toe [35,36].This approach enables accurate

prediction of local stresses while keeping the computational cost at a reasonable level. Table 2 provides an overview of the finite element models investigated in this study.

Table 2: Description of FE models

Model	Scanner	Point spacing	Reconstruction Depth D / Filtering L	FEM Mesh size	FEM Shape function * fully/ reduced integration
M1	FLP	30 [µm]	D10	0.06	quadratic, fully integrated
M1R	FLP	30 [µm]	D10	0.06	quadratic, reduced integrated
M2	FLP	30 [µm]	D10	0.06	linear, fully integrated
M2R	FLP	30 [µm]	D10	0.06	linear, reduced integrated
M3	FLP	30 [µm]	D10	0.12	quadratic, fully integrated
M3R	FLP	30 [µm]	D10	0.12	quadratic, reduced integrated
M4	FLP	30 [µm]	D10	0.12	linear, fully integrated
M4R	FLP	30 [µm]	D10	0.12	linear, reduced integrated
M5	FLP	30 [µm]	D12	0.06	quadratic, fully integrated
M5R	FLP	30 [µm]	D12	0.06	quadratic, reduced integrated
M6	FLP	30 [µm]	D12	0.06	linear, fully integrated
M6R	FLP	30 [µm]	D12	0.06	linear, reduced integrated
M7	FLP	30 [µm]	D14	0.06	quadratic, fully integrated
M7R	FLP	30 [µm]	D14	0.06	quadratic, reduced integrated
M8	FLP	30 [µm]	D14	0.06	linear, fully integrated
M8R	FLP	30 [µm]	D14	0.06	linear, reduced integrated
M9	FLP	60 [µm]	D10	0.06	quadratic, fully integrated
M9R	FLP	60 [µm]	D10	0.06	quadratic, reduced integrated
M10	FLP	60 [µm]	D10	0.06	linear, fully integrated
M10R	FLP	60 [µm]	D10	0.06	linear, reduced integrated
M11	FLP	60 [µm]	D10	0.12	quadratic, fully integrated
M11R	FLP	60 [µm]	D10	0.12	quadratic, reduced integrated
M12	FLP	60 [µm]	D10	0.12	linear, fully integrated
M12R	FLP	60 [µm]	D10	0.12	linear, reduced integrated
M13	FLP	60 [µm]	D12	0.06	quadratic, fully integrated
M13R	FLP	60 [µm]	D12	0.06	quadratic, reduced integrated
M14	FLP	60 [µm]	D12	0.06	linear, fully integrated
M14R	FLP	60 [µm]	D12	0.06	linear, reduced integrated
M15	FLP	60 [µm]	D12	0.12	quadratic, fully integrated
M15R	FLP	60 [µm]	D12	0.12	quadratic, reduced integrated
M16	FLP	60 [µm]	D12	0.12	linear, fully integrated
M16R	FLP	60 [µm]	D12	0.12	linear, reduced integrated
M17	FLP	60 [µm]	D14	0.06	quadratic, fully integrated
M17R	FLP	60 [µm]	D14	0.06	quadratic, reduced integrated
M18	FLP	60 [µm]	D14	0.06	linear, fully integrated
M18R	FLP	60 [µm]	D14	0.06	linear, reduced integrated
M19	FLP	60 [µm]	D14	0.12	quadratic, fully integrated
M19R	FLP	60 [µm]	D14	0.12	quadratic, reduced integrated
M20	FLP	60 [µm]	D14	0.12	linear, fully integrated
M20R	FLP	60 [µm]	D14	0.12	linear, reduced integrated
M21	LLS	full	L0.15	0.06	quadratic, fully integrated
M21R	LLS	full	L0.15	0.06	quadratic, reduced integrated
M22	LLS	full	L0.15	0.06	linear, fully integrated
M22R	LLS	full	L0.15	0.06	linear, reduced integrated
M23	LLS	full	L0.3	0.06	quadratic, fully integrated
M23R	LLS	full	L0.3	0.06	quadratic, reduced integrated
M24	LLS	full	L0.3	0.06	linear, fully integrated

M24R	LLS	full	L0.3	0.06	linear, reduced integrated
M25	LLS	full	L0.6	0.06	quadratic, fully integrated
M25R	LLS	full	L0.6	0.06	quadratic, reduced integrated
M26	LLS	full	L0.6	0.06	linear, fully integrated
M26R	LLS	full	L0.6	0.06	linear, reduced integrated
M27	LLS	half	L0.15	0.06	quadratic, fully integrated
M27R	LLS	half	L0.15	0.06	quadratic, reduced integrated
M28	LLS	half	L0.15	0.06	linear, fully integrated
M28R	LLS	half	L0.15	0.06	linear, reduced integrated
M29	LLS	half	L0.3	0.06	quadratic, fully integrated
M29R	LLS	half	L0.3	0.06	quadratic, reduced integrated
M30	LLS	half	L0.3	0.06	linear, fully integrated
M30R	LLS	half	L0.3	0.06	linear, reduced integrated
M31	LLS	half	L0.6	0.06	quadratic, fully integrated
M31R	LLS	half	L0.6	0.06	quadratic, reduced integrated
M32	LLS	half	L0.6	0.06	linear, fully integrated
M32R	LLS	half	L0.6	0.06	linear, reduced integrated

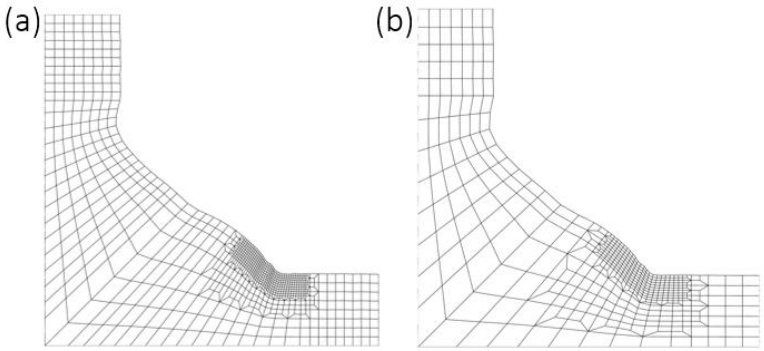


Figure 4: (a) Mesh generation with general resolution 0.06 at weld toe (b) Mesh generation with general resolution 0.12 at weld toe

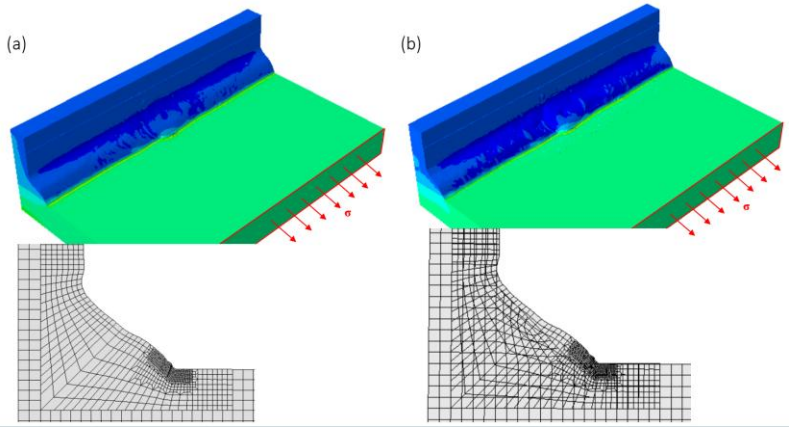


Figure 5: (a) FE model M5 generated by tie connection with cross section at position 50.6 (b) FE model M5 generated by submodeling with cross section at position 50.6

4. Results

4.1 Digitalization

Figure 6 shows the comparison between the raw scan data and the profile obtained after surface reconstruction at the middle of the specimen, at position 59.95. The raw scan data are shown in blue, while the reconstructed surface profile is shown in red and both at a sampling rate of 1:10 for a better illustration. The two profiles follow the same overall geometry, indicating that the surface reconstruction preserves the original profile well. No significant difference is observed between the raw scan data and the reconstructed profile.

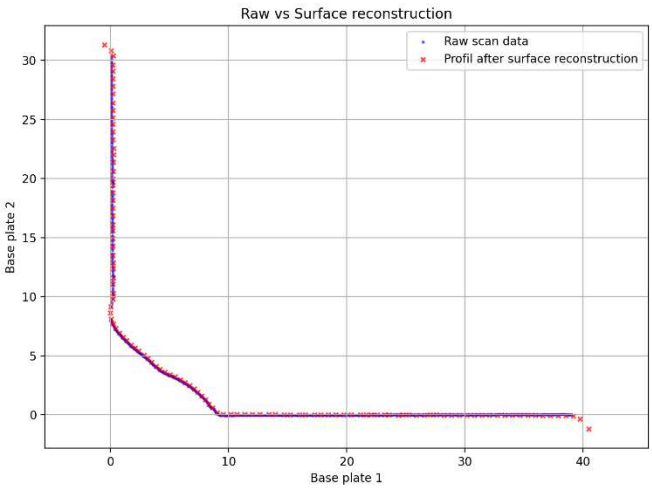


Figure 6: Comparison between the raw scan data (blue) and the surface reconstruction profile (red), shown with a sampling rate of 10

4.2 Data preparation

To assess the influence of the scanning system and preprocessing workflow on the resulting weld geometry, Figure 7 compares the scans from the FLP-based reconstruction and the LLS/Winteria measurement, respectively, after applying the corresponding filtering procedures. Despite the different sensing principles and processing chains, the resulting profiles show very similar weld contours; only small local deviations in surface roughness and toe detail are observed, while the weld toe is essentially unaffected. On this basis, the influence of the chosen scanning system and filtering method on the global weld geometry is considered small, and both approaches are regarded as suitable for providing geometric input to the subsequent FE modelling presented in the next part.

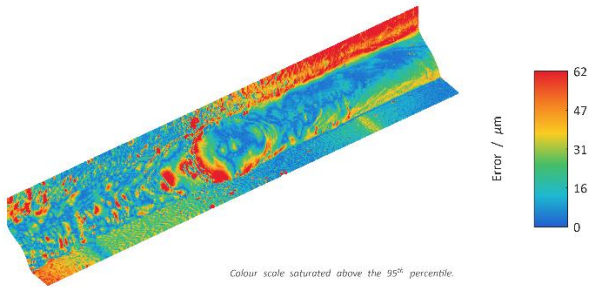


Figure 7: Comparison of the scans from FLP and LLS scanners

4.3 Finite element modelling

The distributions of the maximum principal stress along the weld toe surface obtained with tie constraints are summarized in Figure 8 for FLP scanner and in Figure 9 for LLS scanner. The results are shown for different point spacing (30 µm and 60 µm for FLP; half and full native resolution for LLS), surface filtering parameters (L0.15, L0.3, L0.6), reconstruction depth (D10, D12, D14), mesh sizes (res0.06 and res0.12), and element types (quadratic, fully integrated; quadratic, reduced integrated; linear, fully integrated; linear, reduced integrated).

For the FLP-based models Figure 8, a direct comparison of the paired violin plots for point spacings with 30 µm and 60 µm point spacing shows that the maximum principal stress obtained with the 30 µm scans are generally slightly higher than those based on the 60 µm scans. This difference becomes more evident when the reconstruction depth reaches D12 and D14 with mesh size res0.06, where the local geometry of the weld toe is better resolved and stress concentrations are captured more accurately. At D10, in contrast, the maximum stress values for 30 µm and 60 µm scans are almost identical, indicating that the influence of point spacing is limited when the reconstruction is relatively coarse. If we compare horizontally across different reconstruction depths, it can be concluded that D10 is not sufficient to obtain reliable results, whereas D12 and D14 yield similar stress distributions and are therefore recommended for accurate assessment of weld toe stresses. In addition, the mesh size also has a noticeable influence: for otherwise identical modelling parameters, the coarser mesh (res0.12) systematically leads to lower SCF values than the finer mesh (res0.06), indicating that a sufficiently fine mesh is required to capture the local stress concentration at the weld toe.

Regarding element type, it is evident that the calculated stress level tends to decrease when the element formulation is changed from quadratic to linear (e.g. comparing the blue and orange plots) and further decreases when switching from full integration to reduced integration (e.g. comparing the blue and green plots). Thus, among the tested options, the quadratic, fully integrated element is preferred. This is consistent with general FE practice: for problems focusing on surface stress and local stress gradients, full integration and quadratic interpolation provide a more accurate representation of bending and stress concentration effects, while linear elements are known to be too stiff in bending and may underestimate peak stresses near notches or weld toes [36,37]. Reduced-integration elements can be advantageous for modelling bulk or inner stresses and reducing computational cost, but they are more prone to numerical artefacts such as hour-glassing and may smooth out local stress peaks if the mesh is not sufficiently refined [38].In the present case, where the surface stress distribution along the weld toe is critical for fatigue and fracture assessment, using fine meshes with quadratic, fully integrated solid elements and sufficient reconstruction depth (D12 and D14) is therefore more reliable and is recommended.

For the LLS-based models in Figure 9, the difference between full and half native scan resolution is relatively small, whereas the influence of the surface filtering parameter is much more pronounced. Changes in filtering lead to significant variations in the predicted maximum principal stresses. In addition, for otherwise identical settings, a refinement of the FE mesh systematically increases the stress values, indicating that coarser meshes tend to underestimate the notch stresses due to insufficient geometric resolution. Among the investigated filter lengths, L0.15 is recommended: it yields a stress concentration factor of approximately SCF≈3.7, which is consistent with the values obtained for the FLP-based models under comparable modelling conditions (30 µm point spacing and reconstruction depth 12/14).

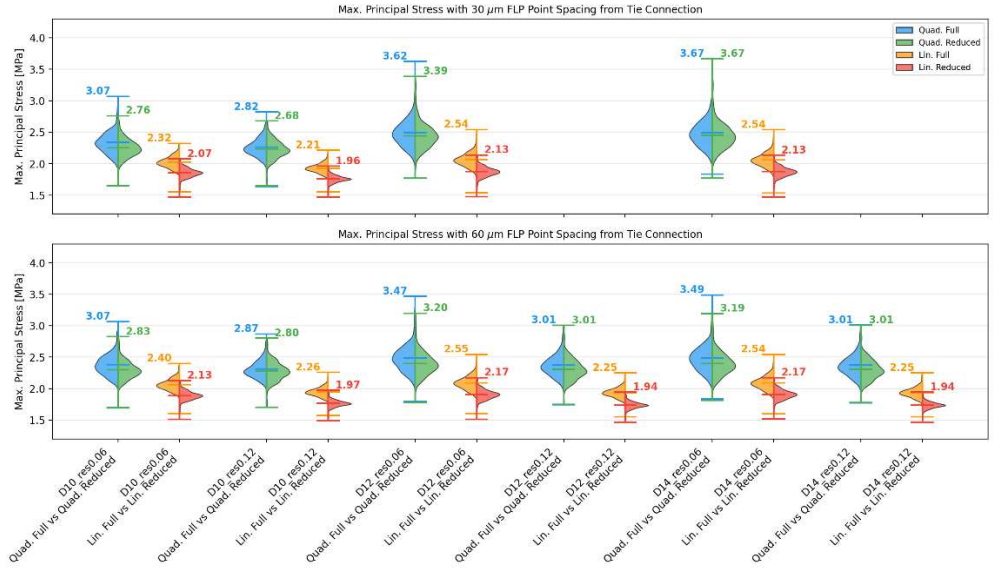


Figure 8: Max. Principal Stress from FLP-based models with TIE connection

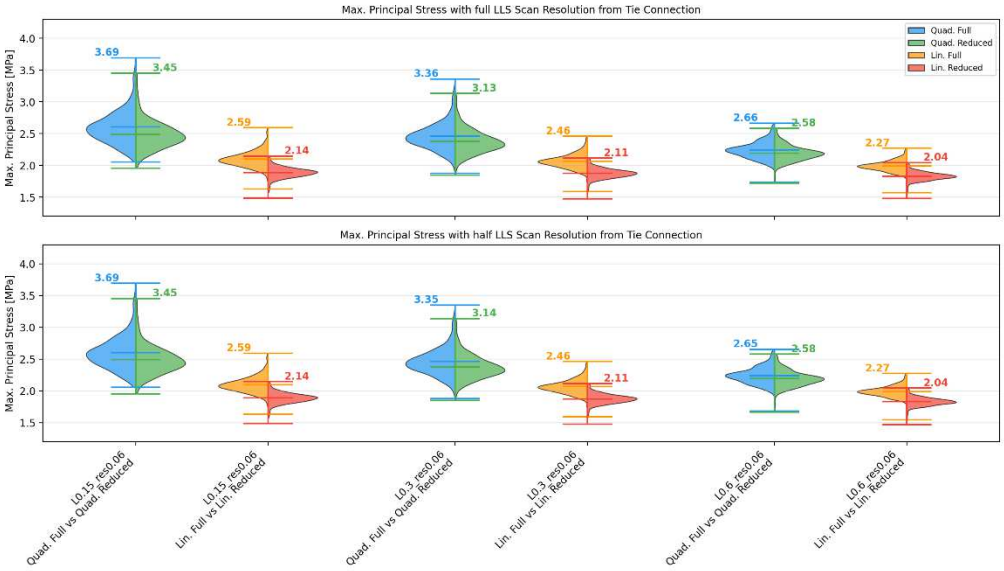


Figure 9: Max. Principal Stress from LLS-based models with TIE connection

In addition, submodeling is also applied to calculate the SCFs, see Figure 10 and Figure 11. A significant finding is that all the SCFs obtained from submodeling are about 0.2–0.3 higher than those evaluated with TIE connections. The main reason is that submodeling allows a much finer local mesh and a more detailed representation of the weld-toe geometry within a smaller domain, so the local stress gradient and notch effects are captured more accurately. In contrast, the global TIE-connected models rely on a comparatively coarser discretization and constraint interpolation across the interface, which tends to smooth the stress field and underestimate the peak stresses at the weld toe. [34,35] Apart from this systematic increase in SCF level, the qualitative findings obtained with TIE connections (regarding the influence of scan resolution, reconstruction depth, filtering parameters, mesh size and element type) also hold true for the submodeling analyses.

Figure 12 shows the maximum principal and effective stresses derived from FE model M5 using CDT extraction at different depths from the weld, corresponding to the critical distance calculated according to Equation (1)-(3) in section 2.2. The peak stress decreases from 3.62 MPa at the weld to 1.65 MPa at x = 0.187 mm. As the depth increases, the range of stress distribution narrows, indicating significant stress concentration at the weld that rapidly decays into a more uniform stress field. This smooth and continuous gradient variation confirms that the CDT-based extraction method reliably captures the stress distribution along the depth direction in model M5.

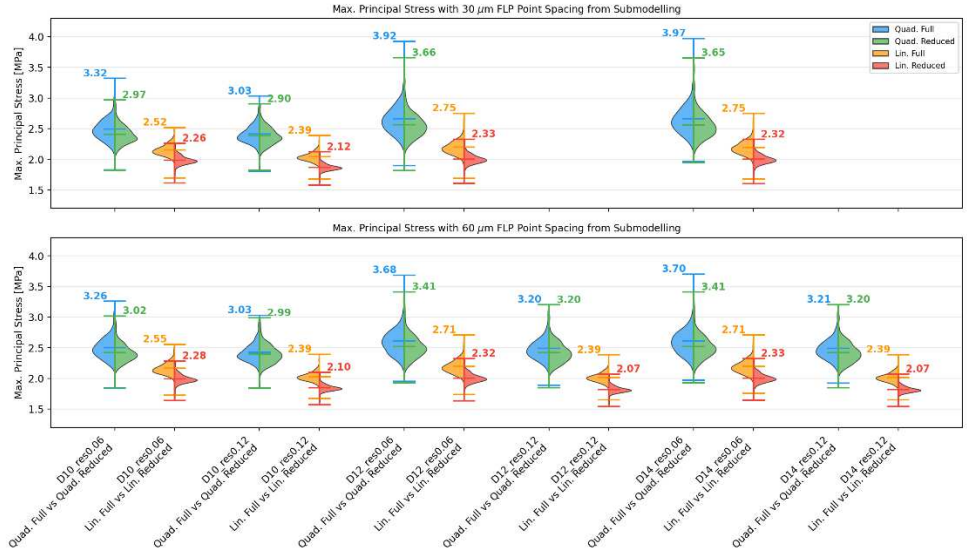


Figure 10: Max. Principal Stress from FLP-based models with Submodeling

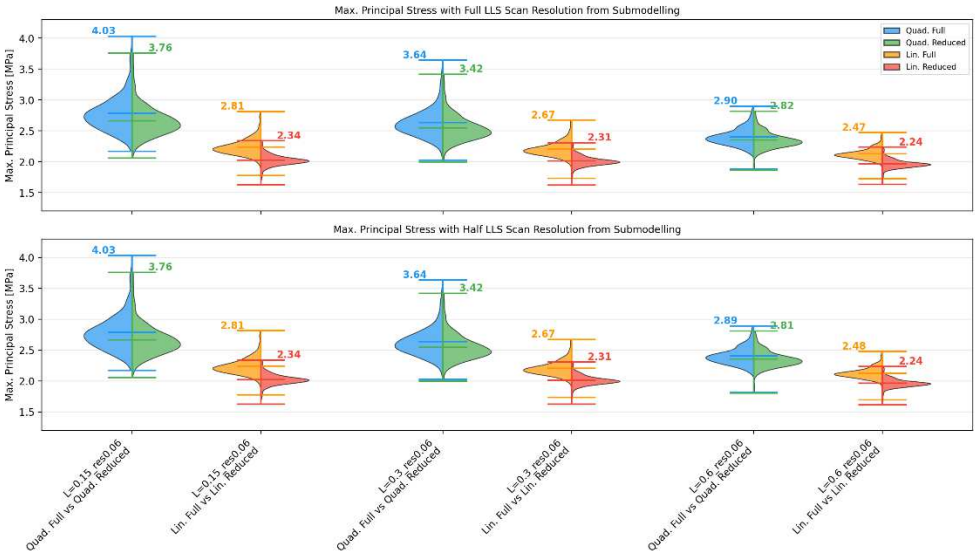


Figure 11: Max. Principal Stress from LLS-based models with Submodeling

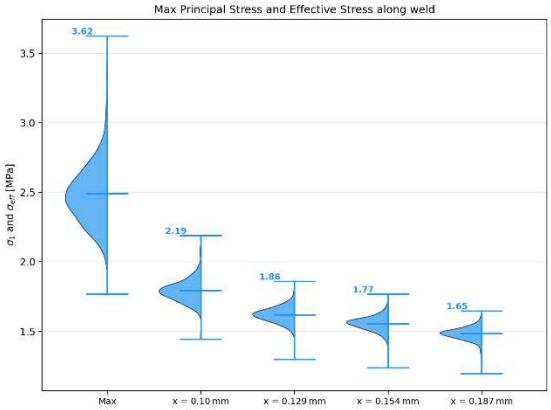
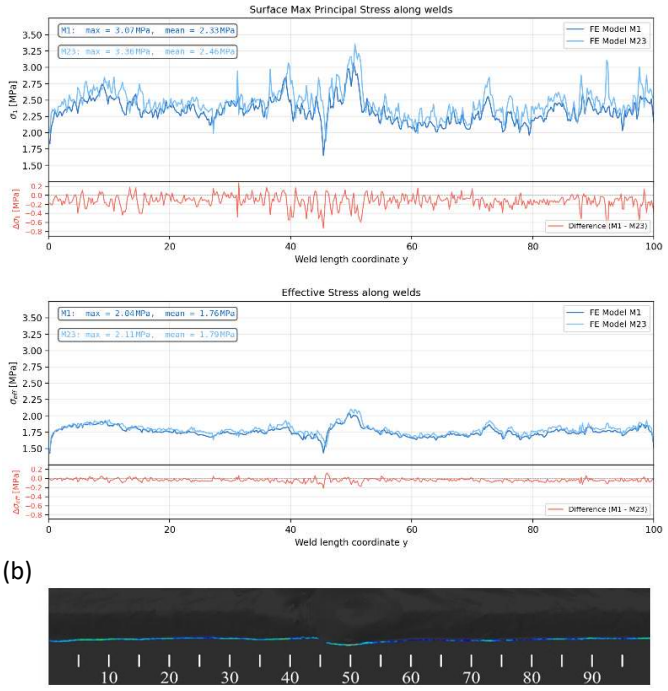


Figure 12: Maximum principal stress $\boldsymbol{\sigma_1}$ and effective stress $\boldsymbol{\sigma_{eff}}$ derived from FE model M5, extracted using CDT at different depths from the weld toe

Figure 13 shows the results of the FE modelling, where two scalar values are obtained from each 0.2 mm cross-section. The upper diagram presents the maximum principal stress σ_1 along the welds for FE models M1 and M23, together with their difference. The lower panel shows the effective stress according to CDT $\sigma_{\text{eff}} = \sigma_1(z = 0.1\ \text{mm})$ for FE models M1 and M23, together with their difference.

One main result that can be taken from Figure 13 is that, although the difference in surface maximum principal stress between the two models is relatively large, the difference in effective stress is much smaller and remains close to zero. This indicates that, when CDT is used, the results obtained from different scanners and FE modelling parameters are consistent and therefore acceptable.

(a)



(b)

Figure 13: Surface Max Principal Stress along welds for FE models M1 and M23 as well as their difference (a, upper); Effective stress according to CDT $\boldsymbol{\sigma_{\text{eff}} = \sigma_1(z = 0.1\ \text{mm})}$ for FE models M1 and M23 as well as their difference (a, lower); Stress distribution and coordinates at the FE model M1. Dark grey color indicate a stress $\boldsymbol{\sigma_1 \leq 2 \times \sigma_n}$ (b)

5. Conclusion

In this study, a comprehensive finite element modelling framework was developed to quantify weld-toe stress concentrations based on 3D surface geometries obtained from two optical scanners (3D fringe light projection sensor and 2D laser line sensor). The workflow systematically combines different point spacings, surface filtering parameters, reconstruction depths, mesh sizes and solid element types to generate global FE models with TIE connections and Submodeling. Surface maximum principal stress along the weld toe and critical distance approach-based effective stress through thickness are extracted from these models, enabling a consistent comparison of the influence of scanner type, geometric reconstruction and finite-element modelling parameters on weld-toe stress assessment within a fracture mechanics framework.

Following conclusions can be made:

- In reverse engineering approach, the reconstruction depth from Poisson Surface Reconstruction and mesh size from finite-element modelling have the strongest influence on the stress concentration factors: increasing the reconstruction depth from D10 to D12/D14 reduces the stress by 15 %, making it the most influential factor, while refining the mesh from 0.12 mm to 0.06 mm results in an 8 % reduction.

- Quadratic and fully integrated solid elements consistently produce higher and more realistic local stress peaks, while longer filters and linear/reduced-integration elements smooth the geometry and stress field, resulting in lower stress concentration factors. Switching from full to reduced integration leads to a 10.5 % reduction in stress, while changing from quadratic to linear elements results in a 23 % reduction.
- Scanner type and point spacing have a comparatively smaller effect on the final stress concentration factors. Submodeling systematically yields higher stress concentration factors than global TIE-connected models with 7.5% difference, but the qualitative trends with respect to the modelling parameters remain the same.
- Although there is a large difference about 8.6% in the maximum principal stress between the models, the effective through-thickness stress based on the critical distance approach is very similar with lower difference about 3%. This quantity can therefore be used as a robust input for further investigations, such as linear elastic fracture mechanics (LEFM) analyses.

Finally, the study demonstrates that the scanner system has only a minor influence, while the FE parameters — primarily the shape function and mesh size — dominate the local stress response at the weld toe.

Future work will focus on experimental validation of the numerically derived SCFs through fatigue testing and fracture mechanics evaluations. In addition, uncertainty quantification of scanner noise, reconstruction settings and FE modelling choices will be carried out to derive robust design SCFs and recommended parameter ranges for industrial applications.

Author contributions: Xiru Wang: writing—original draft, visualization, methodology, software, investigation, formal analysis, conceptualization. Jan Schubnell: conceptualization, supervision. Gustav Hultgren: methodology, software, conceptualization, supervision. Zuheir Barsoum: supervision.

Funding: Open Access funding enabled and organized by Projekt DEAL. This work was part of the project “ORka3D” Grant No. 03EI5019A and funded by the German Federal Ministry for Economic Affairs and Energy (BMWE).

Availability of data: The data of this research is available upon reasonable request.

Declaration of interests: The authors declare no competing interests.

6. References

[1] Hobbacher, A. F. and Baumgartner, J. (2024) *Recommendations for Fatigue Design of Welded Joints and Components*. 3th illust. Springer.

[2] U. Zerbst, M. Madia, M. Vormwald, H. Beier, Fatigue strength and fracture mechanics – ageneral perspective, Engineering Fracture Mechanics 198 (2018) 2–23, fracture mechanics-based determination of the fatigue strength of weldments. https://doi.org/10.1016/j.engfracmech.2017.04.030.

[3] Ninh, Nguyen T., and M. A. Wahab. "The effect of residual stresses and weld geometry on the improvement of fatigue life." *Journal of materials processing technology* 48.1-4 (1995): 581-588.

[4] Lieurade, H. P., I. Huther, and F. Lefebvre. "Effect of weld quality and postweld improvement techniques on the fatigue resistance of extra high strength steels." *Welding in the World* 52.7 (2008): 106-115.

[5] Barsoum, Zuheir, and B. Jonsson. "Influence of weld quality on the fatigue strength in seam welds." *Engineering Failure Analysis* 18.3 (2011): 971-979. https://doi.org/10.1016/j.engfailanal.2010.12.001

[6] Schork, Benjamin, et al. "Effect of the parameters of weld toe geometry on the FAT class as obtained by means of fracture mechanics-based simulations." *Welding in the World* 64.6 (2020): 925-936. https://doi.org/10.1007/s40194-020-00874-7

[7] Hultgren, Gustav, and Zuheir Barsoum. "Fatigue assessment in welded joints based on geometrical variations measured by laser scanning." *Welding in the World* 64.11 (2020): 1825-1831. https://doi.org/10.1007/s40194-020-00962-8

[8] Haibach, Erwin. *Betriebsfestigkeit: Verfahren und Daten zur Bauteilberechnung*. Berlin, Heidelberg: Springer Berlin Heidelberg, 2006. https://doi.org/10.1007/3-540-29364-7_3

[9] Hou, Chien-Yuan. "Computer simulation of weld toe stress concentration factor sequence for fatigue analysis." *International Journal of Structural Integrity* 10.6 (2019): 792-808. https://doi.org/10.1108/IJSI-11-2018-0086

[10] Anthes, R. J., V. B. Köttgen, and T. Seeger. "Kerbformzahlen von stumpfstößen und doppel-t-stößen." *Schweißen und Schneiden* 45.12 (1993): 685-688.
[11] Lawrence, F. V., N. J. Ho, and Pranab Kanti Mazumdar. "Predicting the fatigue resistance of welds." *Annual Review of Materials Science* 11.1 (1981): 401-425. https://doi.org/10.1146/annurev.ms.11.080181.002153
[12] Kiyak, Yusuf, Mauro Madia, and Uwe Zerbst. "Extended parametric equations for weld toe stress concentration factors and through-thickness stress distributions in butt-welded plates subject to tensile and bending loading." *Welding in the World* 60.6 (2016): https://doi.org/1247-1259. 10.1007/s40194-016-0377-x
[13] Schubnell, Jan, et al. "Influence of the optical measurement technique and evaluation approach on the determination of local weld geometry parameters for different weld types." *Welding in the World* 64.2 (2020): 301-316. https://doi.org/10.1007/s40194-019-00830-0
[14] Renken, Finn, et al. "Round-robin study on the determination of weld geometry parameters—part B: analysis of welded specimen." *Welding in the World* 69.8 (2025): 2335-2350. https://doi.org/10.1007/s40194-025-02033-2
[15] Wang, Xiru, Jan Schubnell, and Jörg Baumgartner. "Assessment of stress concentration factors of welded joints based on 2D-and 3D-reverse engineering." *Procedia Structural Integrity* 75 (2025): 85-93. https://doi.org/10.1016/j.prostr.2025.11.010
[16] Ottersböck, M. J., M. Leitner, and M. Stoschka. "Characterisation of actual weld geometry and stress concentration of butt welds exhibiting local undercuts." *Engineering Structures* 240 (2021): 112266. https://doi.org/10.1016/j.engstruct.2021.112266
[17] Randić, Miroslav, Duško Pavletić, and Marko Fabić. "Evaluation of the stress concentration factor in butt welded joints: a comparative study." *Metals* 11.3 (2021): 411. https://doi.org/10.3390/met11030411
[18] Hultgren, Gustav, and Zuheir Barsoum. "Fatigue assessment in welded joints based on geometrical variations measured by laser scanning." *Welding in the World* 64.11 (2020): 1825-1831. https://doi.org/10.1007/s40194-020-00962-8
[19] Niederwanger, A., D. H. Warner, and G. Lener. "The utility of laser scanning welds for improving fatigue assessment." *International Journal of Fatigue* 140 (2020): 105810.
[20] Renken, Finn, et al. "An algorithm for statistical evaluation of weld toe geometries using laser triangulation." *International journal of fatigue* 149 (2021): 106293. https://doi.org/10.1016/j.ijfatigue.2021.106293
[21] Niraula, Abinab, Heikki Remes, and Pauli Lehto. "Local weld geometry-based characterization of fatigue strength in laser-MAG hybrid welded joints." *Welding in the World* 67.6 (2023): 1527-1544. https://doi.org/10.1007/s40194-023-01488-5
[22] Kaffenberger, M., and M. Vormwald. "Application of the notch stress concept to the real geometry of weld end points." *Materialwissenschaft und Werkstofftechnik* 42.4 (2011): 289-297. https://doi.org/10.1002/mawe.201100763
[23] Peterson, R. E. (1959) 'Notch sensitivity', in Sines, G. and Waisman, J. L. (eds) *Metal Fatigue*. New York: McGraw-Hill, pp. 293–306.
[24] Tanaka, K. (1983) 'Engineering formulae for fatigue strength reduction due to crack-like notches', *International Journal of Fracture*, 22(2), pp. R39–R46. doi: 10.1007/BF00942722.
[25] Taylor, D. (1999) 'Geometrical effects in fatigue: a unifying theoretical model', *International Journal of Fatigue*, 21(5), pp. 413–420. doi: 10.1016/S0142-1123(99)00007-9.
[26] Lawrence, F. V. *et al.* (1978) 'Estimating the fatigue crack initiation life of welds', in *Fatigue Testing of Weldments*. Hoeppner,. West Conshohocken, PA: ASTM International, pp. 134–158. https://doi.org/10.1520/STP33393S.
[27] Lawrence, F. V, Ho, N. J. and Mazumdar, P. K. (1981) 'Predicting the Fatigue Resistance of Welds', *Annual Review of Materials Science*, 11(1), pp. 401–425. doi: 10.1146/annurev.ms.11.080181.002153.
[28] Kiyak, Y., Madia, M. and Zerbst, U. (2016) 'Extended parametric equations for weld toe stress concentration factors and through-thickness stress distributions in butt-welded plates subject to tensile and bending loading', *Welding in the World 2016 60:6*, 60(6), pp. 1247–1259. doi: 10.1007/S40194-016-0377-X
[29] Hultgren, G., Mansour, R., & Barsoum, Z. (2023). Fatigue strength assessment of welded joints incorporating the variability in local weld geometry using a probabilistic framework. *International Journal of Fatigue*, *167*, 107364. https://doi.org/10.1016/j.ijfatigue.2022.107364
[30] M. A. Fischler and R. C. Bolles, "Random sample consensus," *Commun. ACM*, vol. 24, no. 6, pp. 381–395, Jun. 1981, doi: 10.1145/358669.358692.
[31] M. Kazhdan, M. Bolitho, and H. Hoppe, "Poisson surface reconstruction," in *Proceedings of the fourth Eurographics symposium on Geometry processing*, 2006, vol. 7, no. 4.
[32] "PoissonRecon/README.md at master · mkazhdan/PoissonRecon · GitHub." https://github.com/mkazhdan/PoissonRecon/blob/master/README.md (accessed Apr. 25, 2025).

[33] Hultgren, G.; Myrén, L.; Barsoum, Z.; Mansour, R. Digital Scanning of Welds and Influence of Sampling Resolution on the Predicted Fatigue Performance: Modelling, Experiment and Simulation. *Metals* **2021**, *11*, 822. https://doi.org/10.3390/met11050822

[34] Dassault Systèmes (2023) Abaqus Analysis User's Guide. Section on tie constraints and constraint equations. Dassault Systèmes, Vélizy-Villacoublay. https://www.3ds.com/products-services/simulia/products/abaqus/

[35] Dassault Systèmes (2023) Abaqus Analysis User's Guide. Section on submodeling analysis. Dassault Systèmes, Vélizy-Villacoublay. https://www.3ds.com/products-services/simulia/products/abaqus/

[36] Cook RD, Malkus DS, Plesha ME, Witt RJ (2001) Concepts and applications of finite element analysis. https://cir.nii.ac.jp/crid/1971149384845029679

[37] Zienkiewicz, Olgierd Cecil, et al. *The finite element method*. Vol. 3. London: McGraw-hill, 1977.

[38] Dassault Systèmes (2023) Abaqus Analysis User's Guide and Abaqus Theory Guide. Dassault Systèmes, Vélizy-Villacoublay. https://www.3ds.com/products-services/simulia/products/abaqus/